



Influences of large-scale convection and moisture source on monthly precipitation isotope ratios observed in Thailand, Southeast Asia

Zhongwang Wei^{a,*}, Xuhui Lee^{a,b}, Zhongfang Liu^c, Uma Seeboonruang^d, Masahiro Koike^e, Kei Yoshimura^{e,f}

^a School of Forestry and Environmental Studies, Yale University, New Haven, CT, USA

^b Yale-NUIST Center on Atmospheric Environment, Nanjing University of Information Science & Technology, Nanjing, Jiangsu, China

^c State Key Laboratory of Marine Geology, Tongji University, Shanghai 200092, China

^d Faculty of Engineering, King Mongkut's Institute of Technology Ladkrabang, Thailand

^e Institute of Industrial Science, The University of Tokyo, Komaba, Tokyo, Japan

^f Atmosphere and Ocean Research Institute, The University of Tokyo, Kashiwa, Chiba, Japan

ARTICLE INFO

Article history:

Received 21 September 2017

Received in revised form 5 February 2018

Accepted 9 February 2018

Available online 6 March 2018

Editor: M. Frank

Keywords:

precipitation isotopes

amount effect

convection

moisture source

Southeast Asia

ABSTRACT

Many paleoclimatic records in Southeast Asia rely on rainfall isotope ratios as proxies for past hydroclimatic variability. However, the physical processes controlling modern rainfall isotopic behaviors in the region is poorly constrained. Here, we combined isotopic measurements at six sites across Thailand with an isotope-incorporated atmospheric circulation model (IsoGSM) and the Hybrid Single-Particle Lagrangian Integrated Trajectory (HYSPPLIT) model to investigate the factors that govern the variability of precipitation isotope ratios in this region. Results show that rainfall isotope ratios are both correlated with local rainfall amount and regional outgoing longwave radiation, suggesting that rainfall isotope ratios in this region are controlled not only by local rain amount (amount effect) but also by large-scale convection. As a transition zone between the Indian monsoon and the western North Pacific monsoon, the spatial difference of observed precipitation isotope among different sites are associated with moisture source. These results highlight the importance of regional processes in determining rainfall isotope ratios in the tropics and provide constraints on the interpretation of paleo-precipitation isotope records in the context of regional climate dynamics.

© 2018 Elsevier B.V. All rights reserved.

1. Introduction

Stable isotope ratios of precipitation have been widely used as hydrological and climatological tracers, due to their variations associated with conditions linked to condensation and evaporation of atmospheric moisture (Cai and Tian, 2016b; Dansgaard, 1964; Gat, 2000; Pfahl et al., 2012; Rozanski et al., 1993; Uemura et al., 2012). For the past 60 years, precipitation isotope ratios have been used for tracking atmospheric water vapor cycling processes at various scales, such as land-atmosphere exchange (Wang et al., 2016a), large-scale transport (Crawford et al., 2013; Dansgaard, 1964; He et al., 2015; Wang et al., 2017; Yoshimura et al., 2003), and cloud-related processes (Cai and Tian, 2016b; Crawford et al., 2017; Pfahl et al., 2012; Wang et al., 2016b, 2017). In addition, the stable isotope records of paleo-precipitation preserved nature archives, such as groundwater (Aggarwal et al.,

2004), ice cores (Pang et al., 2014), speleothems (Liu et al., 2014), lake sediments (Leng and Marshall, 2004) and tree-ring cellulose (Royles et al., 2013), provide unique information relevant to paleoclimate and paleohydrology. All these studies require a good understanding of factors controlling isotope variability of modern precipitation. Furthermore, the isotope information has now been assimilated into a local transform ensemble Kalman filter (LETKF) and the Isotope-incorporated Global Spectral Model (IsoGSM) to constrain both the isotopic fields and the atmospheric dynamic fields (Yoshimura et al., 2014).

Traditional applications in hydrology and paleoclimate studies generally depend on empirical relationships between precipitation isotope compositions and meteorological parameters. One difficulty is that these relationships may vary over time and space, especially in tropical and mid-latitude regions (Breitenbach et al., 2010; Rozanski et al., 1993; Xie et al., 2011; Yang et al., 2012). At middle and high latitudes, the most well-known isotope/climate relationship is the linear dependence of precipitation $\delta^{18}\text{O}$ on temperature (the temperature effect), while in many tropical and monsoon regions, an inverse relationship between precipitation $\delta^{18}\text{O}$ and pre-

* Corresponding author.

E-mail addresses: zhongwang007@gmail.com, zhongwang.wei@yale.edu (Z. Wei).

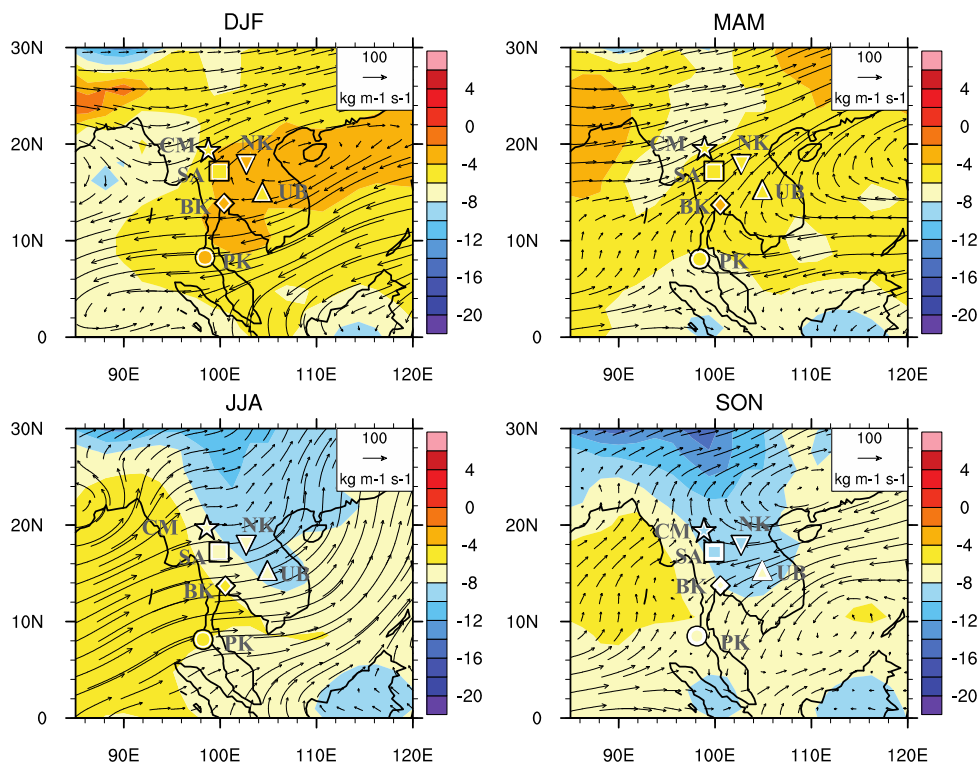


Fig. 1. IsoGSM-simulated spatial distribution of seasonal means of vertical integral water vapor (water vapor transport integrated between the surface layer to 300 hPa level) transport (plotted as vectors) and precipitation isotope ratios (plotted as shading) from 2003 to 2013. (For interpretation of the colors in the figure(s), the reader is referred to the web version of this article.)

precipitation amount (the amount effect) has been observed on the monthly time scale. Additionally, precipitation $\delta^{18}\text{O}$ is also sensitive to changes in the moisture origin (the source effect) and to the integrated histories of both condensation and mixing with surface flux (continental recycling) during the transport of the air mass from the source to the precipitation site (Risi et al., 2013; Zwart et al., 2016). Furthermore, isotopic enrichment of rain droplets occurs below the cloud base when droplets evaporate (Risi et al., 2010; Tremoy et al., 2014).

In the Southeast Asia monsoon region, the amount effect has often been invoked to explain isotopic variability of precipitation at the monthly time scale (Araguás-Araguás et al., 1998; Breitenbach et al., 2010; Cai and Tian, 2016b; Dansgaard, 1964; Lekshmy et al., 2014; Yoshimura et al., 2003). However, there are exceptions to this inverse relationship (Kurita et al., 2009; Rozanski et al., 1993; Tang et al., 2015; Yang et al., 2012). Recent studies suggest that precipitation isotopes in this region are clearly related to regional processes rather than to local precipitation amount (Kurita et al., 2009; Rozanski et al., 1993; Tang et al., 2015; Yang et al., 2012). Large-scale convection and moisture sources probably play an important role in the variability of the isotopic composition of precipitation (Cai and Tian, 2016b; Tang et al., 2015). Other processes associated with cloud microphysics such as cloud-top pressure (CTP) and cloud-top temperature (CTT) also alter the precipitation isotope ratios observed on the ground (Cai and Tian, 2016b). Globally, stratiform rainfall fraction (SRF) has been found to be more negatively correlated with precipitation $\delta^{18}\text{O}$ than local precipitation amount (Aggarwal et al., 2016).

These studies have improved our understanding of precipitation isotope systematics of modern precipitation in Southeast Asia. However, as mentioned above, the associated mechanisms still remain a subject of debate. In particular, uncertainties still exist about climate-isotope relationships over time and space, as well as the degree to which climate variables manifest themselves in pre-

cipitation isotopes both at the local and at the regional scale. This is partly because isotope records available are too sparse in space and their lengths too short to resolve the spatial and temporal variability of precipitation isotopic composition in this region. In the Global Network of Isotopes in Precipitation (GNIP), multi-year records of precipitation $\delta^{18}\text{O}$ in this region only exist for Bangkok.

In this study, monthly precipitation isotope records from a network of 6 sites across Thailand are analyzed. This analysis is supported by IsoGSM simulations and back trajectory calculations. We aim to identify atmospheric processes that control the precipitation isotope ratios in this region, improving the interpretation of paleo-isotope records.

2. Data and methods

2.1. Site and measurement

Precipitation isotope data was obtained from a network of six sites evenly distributed in Thailand, including Bangkok (BK), Chiang Mai (CM), Nong Khai (NK), Phuket (PK), Si Samrong Agromet (SA) and Ubon Ratchathani (UB) (Fig. 1 and Table 1). This monitoring network was launched by the University of Tokyo in 2002 and was designed to provide sampling of water isotopes (δD and $\delta^{18}\text{O}$) on a daily basis. Between 2002 and 2014, a total of 5239 samples were analyzed in the University of Tokyo Hydrological Laboratory, using a Picarro cavity ring-down spectrometer (model L2120-i). The measurement was normalized to the Vienna Standard Mean Ocean Water and the Standard Light Antarctic Precipitation (VSMOW-SLAP) scale using a two-point linear calibration generated from reference waters supplied by IAEA, with an analytical precision and accuracy of $\pm 0.1\text{‰}$ for $\delta^{18}\text{O}$ and $\pm 1.3\text{‰}$ for δD . Detailed information about field sampling and the laboratory procedure is described in Wei et al. (2016). The monthly precipitation δD and $\delta^{18}\text{O}$ are amount-weighted (Online Supplementary Information). The daily samples that were likely influenced by

Table 1

Statistical summary of monthly amount weighted precipitation isotopic ratios for each site. The months in parentheses indicate the time when the extreme δ value occurred.

Site	Lon. (°E)	Lat. (°N)	Elevation (m)	Number of samples	Sampling period	$\delta^{18}\text{O}$			δD		
						Min	Max	Ave.	Min	Max	Ave.
Phuket (PK)	98.3	8.1	9	808	2003–2009	−9.1 (Oct.)	1.4 (Jan.)	−5.8	−61.3	11.8	−35.2
Bangkok (BK)	100.6	13.7	6	559	2003–2011	−13.5 (Oct.)	−0.6 (Apr.)	−6.3	−98.1	4.9	−41.2
UBon Ratchathani (UB)	104.9	15.3	127	625	2003–2015	−11.9 (Sep.)	0.3 (Apr.)	−7.6	−84.9	12.1	−52.1
Si Samrong Agromet (SA)	99.9	17.2	54	511	2002–2015	−14.2 (Sep.)	−1.5 (Apr.)	−7.7	−44.3	2.7	−53.2
Nong Khai (NK)	102.7	17.9	175	769	2003–2015	−14.0 (Sep.)	−0.9 (Apr.)	−7.6	−103.0	7.1	−51.9
Chiang Mai (CM)	99.0	18.8	313	818	2003–2015	−12.9 (Sep.)	1.7 (Apr.)	−7.2	−102.5	11.4	−48.1

evaporation have been discarded from the amount-weighted calculation. Our data screening criteria are: (1) rainfall amount is less than 3 mm; (2) deviation of $\delta^{18}\text{O}$ from the LMWL (Local Meteoric Water Line) is greater than 5‰. On the monthly timescale, we further excluded those months during which the collected precipitation amount is lower than 80% of the total precipitation amount due to missing collection on some precipitation days. More details about the samples used in this study are summarized in Table 1.

2.2. Meteorological and other supporting data

Besides in-situ meteorological and isotopic data, satellite and other data products were used to understand how large-scale processes control the variability of precipitation $\delta^{18}\text{O}$. The monthly regional precipitation surrounding each site was obtained from the Global Precipitation Climatology Project (GPCP) Version 2 dataset (Adler et al., 2003). The GPCP dataset with a 2.5×2.5 degree resolution is based on gauge and satellite observations. NOAA monthly Outgoing Longwave Radiation (OLR), with gaps filled with temporal and spatial interpolation schemes given by Liebmann and Smith (1996), was used to investigate regional convective activity. Data obtained from high-spectral resolution measurements made by the Atmospheric Infrared Sounder onboard the Earth Observing System Aqua satellite (Kahn et al., 2008) was used to explore linkages between precipitation $\delta^{18}\text{O}$ variability and CTP and CTT. Stratiform rainfall fraction (SRF), defined as the ratio of stratiform volumetric rainfall to total volumetric rainfall (Aggarwal et al., 2016), was calculated using NASA's tropical Rainfall Measuring Mission (TRMM) PR 2A25 V7 data products (Funk et al., 2013) for each site with a horizontal resolution of 0.5×0.5 degree.

2.3. IsoGSM simulations

IsoGSM, which is a water isotope-enabled general circulation model (Yoshimura et al., 2008), was used to explore how synoptic weather cycles control monthly $\delta^{18}\text{O}$ variability at each of the six observation sites. IsoGSM has a horizontal resolution of about 200 km and 28 vertical levels, and a time resolution of six hours. The spectral nudging technique is used to constrain the model results with the NCEP/NCAR Reanalysis 2 data. In IsoGSM, isotopic fractionation occurs during phase transition processes. The isotopic fractionation is assumed to be in thermodynamic equilibrium, except for open water evaporation, condensation in supersaturation conditions (vapor to ice), rain drop re-evaporation and air-rain isotopic exchange, where kinetic fractionation occurs. A constant isotopic value of 0‰ is assumed for the ocean water. No fractionation occurs in land surface evapotranspiration. A detailed description of

the model setup can be found in Yoshimura et al. (2008, 2014) and Wei et al. (2016). IsoGSM uses the spectral nudging technique (Yoshimura et al., 2008) that allows it to be constrained by the actual atmospheric thermodynamic situation. IsoGSM can reproduce reasonably well monthly variabilities of precipitation and water vapor isotopic compositions associated with synoptic weather cycles, and its products have been validated by (Farlin et al., 2013; Wei et al., 2016).

2.4. Back-trajectory analysis

Air mass back-trajectories were retrieved from the Hybrid Single-Particle Lagrangian Integrated Trajectory (HYSPPLIT) model version 4.0 (Adler et al., 2003; Draxler and Hess, 1997; Stein et al., 2015). The global NOAA-NCEP/NCAR reanalysis data was used for tracing air masses. Trajectories were computed for an end height of 1500 m above the mean sea level, an expected height of rain formation in this region (Aggarwal et al., 2004; Breitenbach et al., 2010), for a time period of 10 days, which is the mean residence time of moisture in the troposphere (Gat, 2000; Trenberth, 1998). For each rainwater-sampling day at each site, backward trajectories were calculated at 6-h intervals to help identify changes of the source region. The specific humidity along the backward trajectory was also calculated to account for precipitation and evaporation processes during water vapor transport (Crawford et al., 2017, 2013; Sodemann et al., 2008; Wang et al., 2017). At each 6-h interval, if the specific humidity along the trajectory was lower than 0.05 g/kg, the trajectory was terminated. If the specific humidity at the present time interval was higher (lower) than at the previous time interval, the location of air parcel at the previous time was marked as an evaporation (condensation) location (Sodemann et al., 2008; Wang et al., 2017). To quantify the relationship between moisture sources and precipitation $\delta^{18}\text{O}$, we estimated the moisture evaporated into the air from time change of absolute humidity when the back trajectory passed over the specified region. There were three moisture source regions: Pacific Ocean (east of 100°E), Indian Ocean (west of 100°E) and land surface. The monthly contribution from each source region was calculated by the sum of moisture coming from that region and further weighted by the precipitation recorded at the measurement site. The moisture source analysis is presented in Sec. 3.3. Similar approaches have been used to identifying moisture sources in various climatic conditions, including Greenland (Sodemann et al., 2008), Australia (Crawford et al., 2017, 2013), Central Asia (Wang et al., 2016a, 2017) and Switzerland (Aemisegger et al., 2014). The model was further modified to allow us to trace other variables such as OLR or $\delta^{18}\text{O}$ of precipitable water simulated by the IsoGSM.

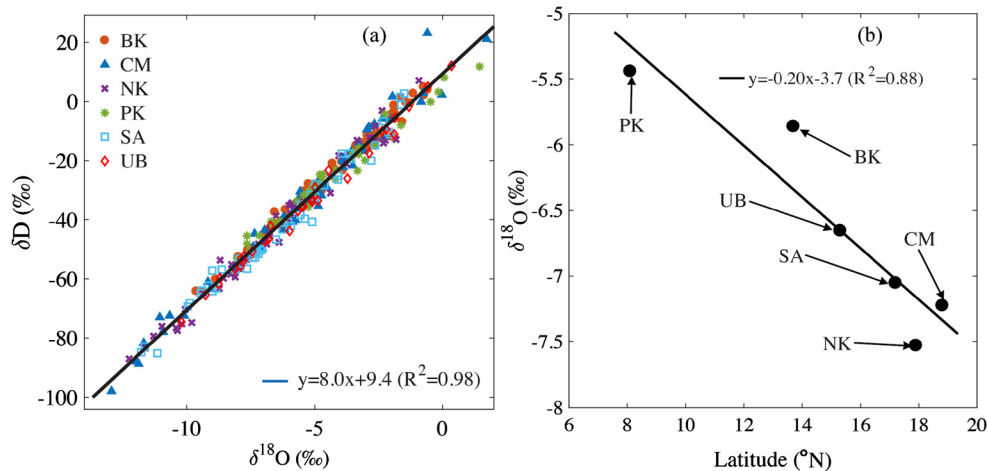


Fig. 2. a) $\delta^{18}\text{O}$ – δD diagram of the water samples (precipitation weighted monthly averaged) collected for this study. The black linear fit indicates the LMWL; b) Annual amount-weighted mean precipitation $\delta^{18}\text{O}$ at each site plotted against latitude.

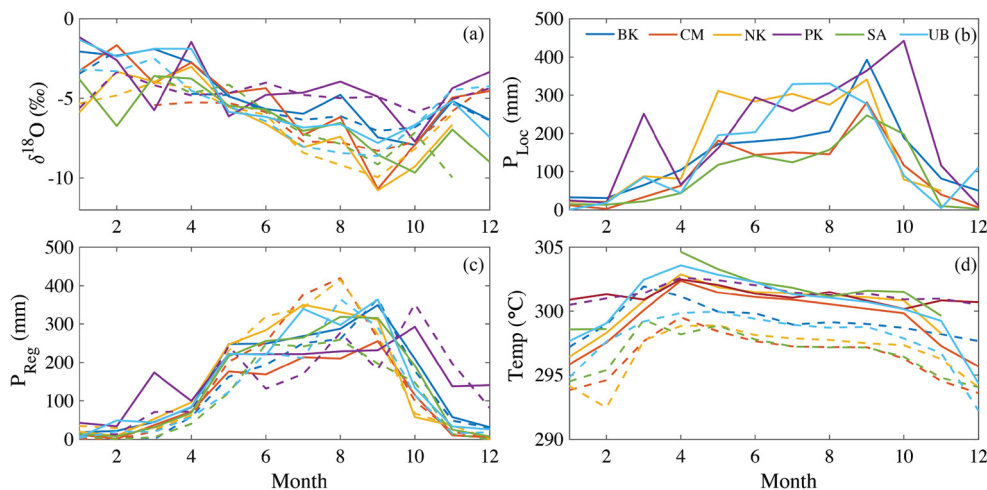


Fig. 3. Multi-year mean seasonal variations of measured (solid lines) and IsoGSM simulated (dash lines) precipitation $\delta^{18}\text{O}$, precipitation amount, GPCP grid precipitation amount and air temperature.

3. Results and discussion

3.1. General patterns

The precipitation $\delta^{18}\text{O}$ and the vertically integrated water vapor amount simulated by IsoGSM are shown in Fig. 1. During the DJF (December, January and February) season, the precipitation was generally controlled by moisture from the Pacific Ocean, while a higher contribution of moisture from the Indian Ocean can be found for the JJA (June, July and August) season. The precipitation $\delta^{18}\text{O}$ values generally decreased along the monsoon track in these seasons. On the other hand, the moisture source varied among the sites for the MAM (March, April and May) and SON (September, October and November) seasons and thus resulted in more complicated spatial variations of precipitation $\delta^{18}\text{O}$.

A least squares regression of amount-weighted $\delta^{18}\text{O}$ and δD values for all stations shows that the LMWL is $\delta\text{D} = 8\delta^{18}\text{O} + 9.4$ ($R^2 = 0.98$, $p < 0.01$) (Fig. 2), which is almost the same as the Global Meteoric Water Line (GMWL, $\delta\text{D} = 8\delta^{18}\text{O} + 10$; Craig, 1961). The LMWL suggests that overall these samples have not been significantly affected by sub-cloud evaporation. As the $\delta^{18}\text{O}$ and δD values are highly linearly correlated, the following results are given in terms of $\delta^{18}\text{O}$ only. d-Excess, defined as $d = \delta\text{D} - 8\delta^{18}\text{O}$ (Dansgaard, 1964), was also calculated for tracing moisture region.

A statistical summary of the measured isotopic values for each station is presented in Table 1. Rainfall isotope ratios show a large range of variations over the observation period, with maximal monthly value at CM (1.7‰) and minimal value at SA (−14.2‰). Generally, the maximum δ was observed in April, except for PK where the maximum occurred in January, while the minimum δ value occurred in September and October. There was a tendency of larger temporal ranges with increasing latitude. In spite of these large temporal variations, these stations exhibited similar isotope averages, with gradually depleted isotope values towards higher latitudes (Fig. 2). The average gradient was -0.2‰ per degree of latitude change, which is much smaller than value of -0.6‰ per degree reported for the mid-latitudes (Mook, 2000).

3.2. Local controls on seasonal variability of precipitation $\delta^{18}\text{O}$

The climatology of monthly precipitation $\delta^{18}\text{O}$, local precipitation amount, GPCP grid-level precipitation amount and local air temperature are shown in Fig. 3. The majority (>82%) of annual rainfall occurred in active monsoon months (May to September) during which rainfall was more depleted in ^{18}O (Fig. 3b and 3c). Higher precipitation $\delta^{18}\text{O}$ values were observed in the winter and early spring; Precipitation $\delta^{18}\text{O}$ showed a gradual decrease with time after onset of the summer Asia monsoon (Fig. 3a). This temporal pattern of precipitation isotope is consistent with previ-

Table 2

Correlation coefficients between monthly precipitation $\delta^{18}\text{O}$, IsoGSM simulated precipitation $\delta^{18}\text{O}$, local precipitation amount (P_{local}), GPCP grid precipitation amount (P_{regional}), local air temperature (T), cloud-top pressure (CTP), cloud-top temperature (CTT), outgoing longwave radiation (OLR), and stratiform rainfall fraction (SRF).

Station	Number	IsoGSM	P_{local}	P_{regional}	T	CTP	CTT	OLR	SRF
BK	64	0.75 ^a	−0.60 ^a	−0.66 ^a	0.14	0.28	0.19	0.64 ^a	0.15
CM	54	0.69 ^a	−0.62 ^a	−0.62 ^a	0.05	0.14	0.21	0.47 ^a	0.28
NK	55	0.68 ^a	−0.28 ^b	−0.29 ^b	0.07	0.19	0.15	0.18	0.11
PK	39	0.71 ^a	−0.58 ^a	−0.64 ^a	0.40 ^a	0.25	0.16	0.64 ^a	0.30
SA	51	0.70 ^a	−0.43 ^a	−0.42 ^a	0.12	0.13	0.10	0.16	0.29
UB	37	0.68 ^a	−0.51 ^a	−0.46 ^a	0.15	0.11	0.11	0.42 ^a	0.10

^a $p < 0.01$.

^b $0.01 < p < 0.05$.

ous studies based on the GNIP dataset for the tropical and mid-latitude regions (Aggarwal et al., 2004; Araguás-Araguás et al., 1998; Breitenbach et al., 2010; Cai and Tian, 2016b; Xie et al., 2011). According to these studies, an inverse relationship exists between precipitation $\delta^{18}\text{O}$ and precipitation amount: precipitation $\delta^{18}\text{O}$ typically reaches its minimum in the season of maximum rainfall and its maximum in the season of lowest rainfall. However, neither local precipitation amount nor regional precipitation amount can fully explain the precipitation $\delta^{18}\text{O}$ observed at our sites. For example, SA had a monthly maximum amount of precipitation was observed in September (315.0 mm based on local observation and 247.3 mm based on GPCP), but the $\delta^{18}\text{O}$ minimum was observed in October (−9.7‰) in the off-monsoon season. Similarly, BK, the minimum $\delta^{18}\text{O}$ value (−7.9‰ in October) did not correspond to maximum precipitation (348.9 mm locally and 393.2 mm according to GPCP in September). Similar to $\delta^{18}\text{O}$, monthly precipitation d-excess showed a slightly decrease during the summer monsoon season (Supplementary Fig. S1), whereas large variabilities were observed for other seasons.

The GPCP grid-level precipitation amount and peak time could deviate from the locally measured values. For example, at PK, the October GPCP precipitation value was 100 mm lower than the value observed locally. At NK, the maximum local precipitation occurred in September, whereas the maximum GPCP precipitation was observed in July. These differences suggest that local precipitation may be influenced by local topographic effects in addition to large-scale atmospheric conditions.

Correlation analysis of monthly precipitation $\delta^{18}\text{O}$ with local precipitation amount, near-surface air temperature, and model-derived variables is summarized in Table 2. The correlation between local precipitation amount and precipitation $\delta^{18}\text{O}$ varied among sites. The amount effect appeared more clearly at tropical oceanic stations ($R = -0.60$ at CM and -0.62 at BK, respectively) than at the terrestrial station (e.g. $R = -0.28$ at NK). The results hold true when the GPCP data are used. At coastal sites (BK and PK), strong positive correlations existed between precipitation $\delta^{18}\text{O}$ and OLR. Precipitation $\delta^{18}\text{O}$ exhibit much weaker correlation with the near surface temperature than with other atmospheric variables, in part because the near-surface temperature at these sites did not change significantly with season (Fig. 3d).

The IsoGSM reproduced the precipitation $\delta^{18}\text{O}$ reasonably well at all sites and in terms of both the temporal and spatial variability (Table 2). This was especially true for the rainy seasons when the IsoGSM accurately reproduced the spatial variability of $\delta^{18}\text{O}$ (Fig. 3), which implies that our simulation can reasonably capture the influence of large-scale moisture advection on precipitation $\delta^{18}\text{O}$ variations. In contrast to the $\delta^{18}\text{O}$ values, IsoGSM is less successful with d-excess values, likely associated with the specific physics in the present model (Yoshimura et al., 2008), although its d-excess trends were similar to the observed trends (Supplementary Fig. S1). IsoGSM also predicted precipitation amount very well except for some overestimation at the CM site. The simulated 2-m temperature displayed clear seasonal cycles, consistent with the observations, but with an underestimation of 3 °C for most of

sites. This may be due to the relatively coarse resolution of the IsoGSM that can not resolve the observational sites.

Another factor that influences precipitation/isotope relationships is the well-known post-condensation processes or the interaction between rain drops and the water vapor under the cloud (Kurita et al., 2009). On a monthly timescale, however, the contribution of this effect becomes relatively weak due to the isotopic variability associated with rain-out process in the surrounding region (Kurita et al., 2009). The fact that our $\delta^{18}\text{O}$ and δD were well distributed along the GWML suggests that post-condensation processes played a minor role on the monthly timescale (Fig. 2). Moreover, the high precipitation amount and high relative humidity at our sites would limit the post-condensation effect. This is also supported by a recent ideal simulation study, which suggests that raindrop evaporation does not have a great contribution to the amount effect as was assumed (Moore et al., 2014). As reported previously, local CTP, CTT and SRF are also suggested as indicators of precipitation $\delta^{18}\text{O}$ variability. However, correlation analysis for all sites showed that $\delta^{18}\text{O}$ was largely independent of CTP, CTT and SRF (Table 2). Nevertheless, the difference between these correlations indicates that these commonly-used atmospheric variables, either observed locally or modeled at the grid-level, are insufficient to explain the air mass rainout history and its isotopic variability across space.

3.3. Remote controls

The precipitation $\delta^{18}\text{O}$ depends on the proportion of moisture coming from oceanic evaporation and from land evapotranspiration. Figs. 4 and 5 show examples of back-trajectory simulation results in May and September 2005 for the PK and the NK site, respectively. These two sites were selected because $\delta^{18}\text{O}$ was similar in May but differed significantly in September and because the moisture source at these two sites in 2005 was significantly different from multi-year climatology. The percentage of moisture originating from the land surface, the Indian Ocean and the Pacific Ocean was estimated for each month using the method described in section 2.4. The results show that changes in moisture source were a driver of the observed temporal and spatial $\delta^{18}\text{O}$ variability. At NK, 85% of the moisture came from Indian Ocean in May 2005, while the moisture in September 2005 was a mixture of water vapor originating from the land (52%), the Indian Ocean (28%) and the Pacific Ocean (20%). At the PK site, the main moisture source was the Indian Ocean in May, contributing 88% of the moisture, a proportion similar to that at the NK site. In September, the overwhelming source at the PK site was also the Indian Ocean (87%), while the Pacific Ocean and the land surface played minor roles, contributing only 11% and 2% of the moisture. On the other hand, for the multi-year mean, the Indian Ocean contributed to only about 60% and 6% in May and September at NK, 91% and 75% in May and September at PK, respectively.

The evolutions of specific humidity and isotopic composition of precipitable water along the airmass trajectory are shown in Figs. 4 and 5. The isotopic composition of precipitable water was used

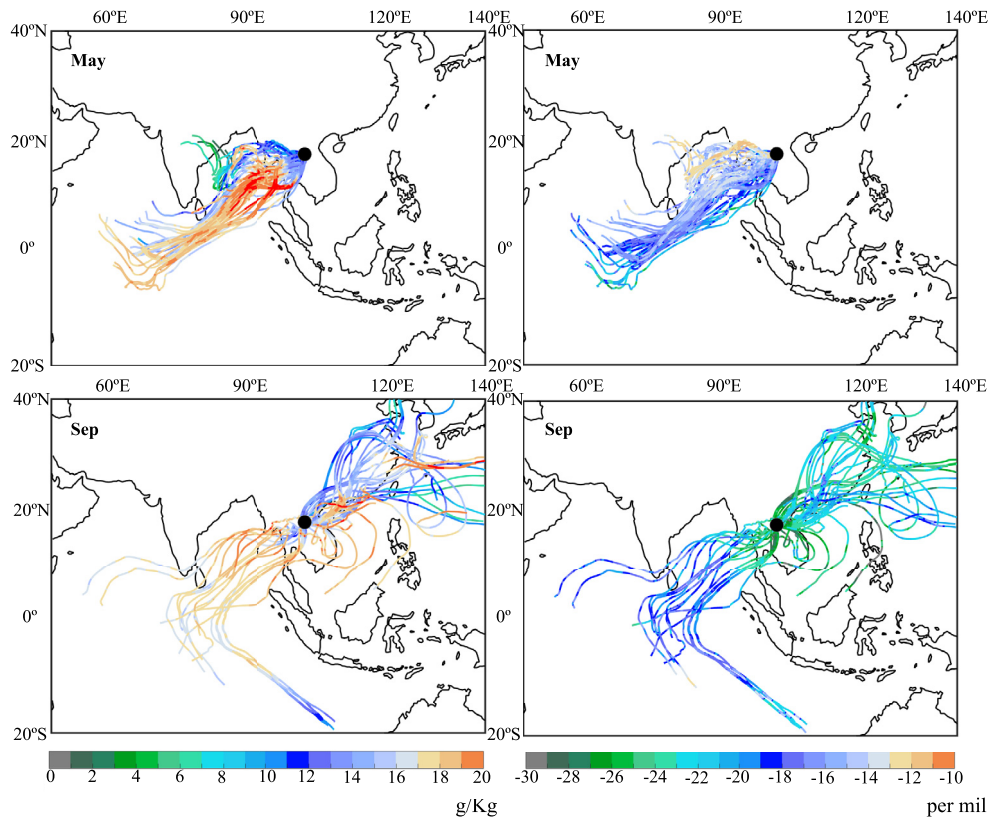


Fig. 4. Backward trajectories at NK site for precipitation days in May and September 2005. Colors indicate specific humidity (left panel) and precipitable water $\delta^{18}\text{O}$ (right panel) along the trajectories.

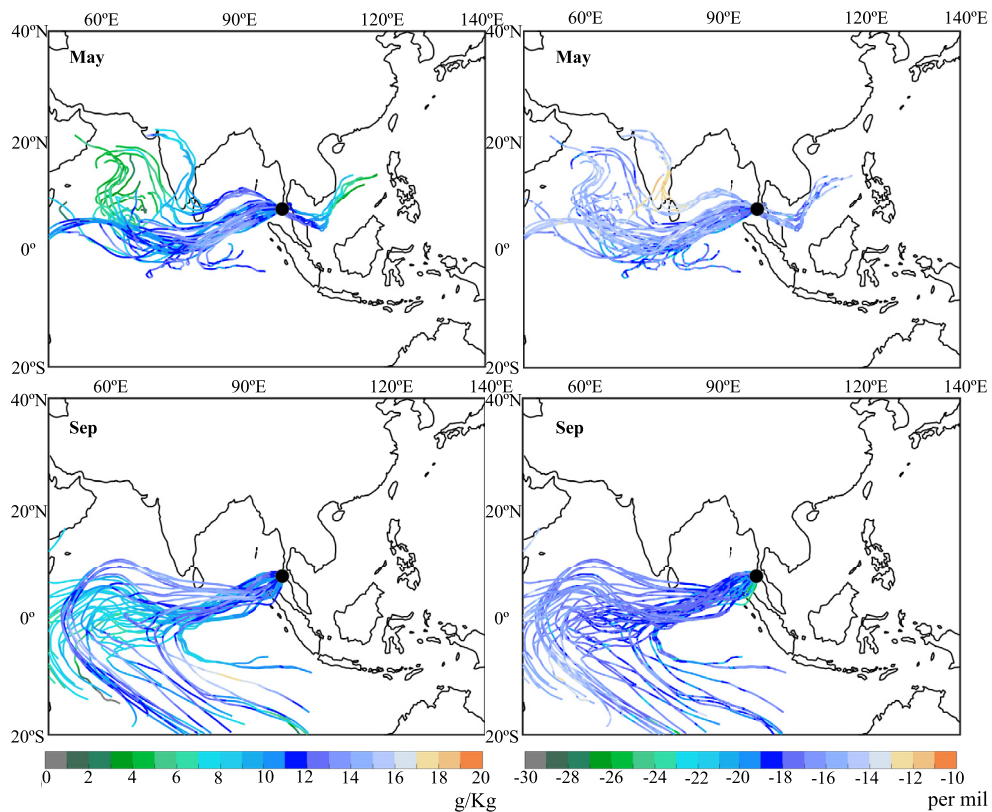


Fig. 5. Backward trajectories for precipitation days calculated for the isotope measurements at the PK site in May and September 2005. Colors indicate specific humidity (left panel) and precipitable water $\delta^{18}\text{O}$ (right panel) along the trajectories.

here instead of precipitation $\delta^{18}\text{O}$ because precipitation did not occur continuously along the trajectory. For NK in May, the moisture forming precipitation was more likely to come from the Bay of Bengal due to strong evaporation in this region (Fig. 4). Although the specific humidity showed a large decrease just before the air mass reaching the southwest coast of Thailand, only minor reduction of $\delta^{18}\text{O}$ of precipitable water was found (Fig. 4). The $\delta^{18}\text{O}$ of precipitable water varied from -22‰ to -10‰ along the whole trajectory. The $\delta^{18}\text{O}$ of precipitable water was much more depleted in September than in May due to a higher contribution of the land source and more rainout before the airmass reached the sampling site in September. For the PK site in May and September (Fig. 5), the dominant moisture sourced from the Bay of Bengal, which is similar to the NK site in May. The specific humidity was initially low at the start of the airmass transport and became higher when the airmass passed through this region and was slightly depleted when the airmass reached the land.

A direct comparison of the isotopic composition of IsoGSM simulated surface evaporation (or evapotranspiration over land; ET) $\delta^{18}\text{O}$ from different source regions (Supplementary Fig. S2) was used to tease apart the relative influence of these different moisture sources on precipitation $\delta^{18}\text{O}$. In May, the ET $\delta^{18}\text{O}$ along the trajectories varied from -6‰ to -4‰ for both the NK and PK sites. In September, there is little change in sources region of precipitation at PK site, while for the NK site, the ET $\delta^{18}\text{O}$ from the dominated source region (land surface) was more depleted (-14‰ to -8‰). These patterns are confirmed by our site-based precipitation isotope measurements, which showed high consistence of amount-weighted monthly $\delta^{18}\text{O}$ averages at PK and NK in May (-4.5‰ and -3.3‰ for PK in May and September, respectively, and -4.1‰ for NK in May) and the isotopically most depleted precipitation at NK in September (-10.9‰). The source impact is also confirmed by the comparison of d-excess simulation from source regions (Supplementary Fig. S3), because d-excess is insensitive to non-moisture source processes such as re-evaporation of rainfall, moisture mixing and convection activity during the distillation process along the vapor transport trajectory. At the NK site, ET d-excess along the trajectories varied from 12‰ to 16‰ and 6‰ to 12‰ in May and September, respectively. At the PK site, the source d-excess is slightly lower than at the NK site, ranging from 8‰ to 12‰ and 4‰ to 12‰ in May and September, respectively. The observed precipitation d-excess in May and September was 14.1‰ and 11.6‰ at NK, 9.9‰ and 8.5‰ at PK, respectively. For the PK site in May and September, the source water is dominated by low-latitude Indian Ocean with relatively low ET d-excess, while moisture for the NK site in May is from high latitude Indian Ocean with high ET d-excess. For the NK site in May, a higher source contribution from the land surface resulted a relatively high d-excess in precipitation. At the same time, the similar differences in the source region ET d-excess and in local precipitation d-excess between these months also indicate that the source had an effect on precipitation isotope ratios.

Fig. 6 shows cluster means of OLR, precipitable water and its $\delta^{18}\text{O}$. The precipitable water $\delta^{18}\text{O}$ values at PK in May and September and at NK in May were generally close to each other, although the cluster means of specific humidity varied in a large range (Supplementary Fig. S4). On the other hand, $\delta^{18}\text{O}$ values for NK in September were most isotopically depleted, although the variability of specific humidity along the trajectory was similar with that in May. This is consistent with ET isotope source analysis introduced above. A significant negative correlation between the OLR measurement and simulated precipitable water content suggests that our model reproduced precipitable water content correctly (Supplementary Fig. S5).

As the air mass moves through the oceanic source region, it may pick up abundant moisture from convective transport along

air mass trajectory, which leads to an increase in precipitable water (Supplementary Fig. S6) and a decrease in ORL due to convective cloud (Supplementary Fig. S7). Although our trajectory calculation can not resolve convective transport, significant correlations of precipitable water $\delta^{18}\text{O}$ with precipitable water ($R^2 > 0.79$) and ORL ($R^2 > 0.79$) suggest that convective activity is a dominant control on precipitation $\delta^{18}\text{O}$ variability along which air mass traveled over the ocean (except for NK site in May, Fig. 6). It is noted that this negative correlation between the amount of precipitable water and its $\delta^{18}\text{O}$ does not reflect the rainout effect, because the rainout effect is associated with depleted $\delta^{18}\text{O}$ in moisture and precipitation due to removal of water vapor as condensate. Instead, this correlation should also be explained by isotopic rainout effect resulted from vertical air motions and microphysical processes governing rain formation through convective activity (Aggarwal et al., 2016). The convective-driven rainout can result in $\delta^{18}\text{O}$ -depleted water vapor at low levels which then feeds the subsequent convective systems with lower $\delta^{18}\text{O}$ (Lawrence et al., 2004; Risi et al., 2008, 2010). However, though this rainout process lowers the $\delta^{18}\text{O}$ value of precipitable water, it does not decrease atmospheric humidity (left panel in Fig. 6). This may reflect the variability in the balance of rainout and ocean-surface recycling for air mass moving across ocean. When rainout effect exceeds convective recycling, the atmospheric humidity decreases, and vice versa. This appears to be supported by the evolution of the specific humidity along air mass trajectory (Supplementary Fig. S4). During air mass transport from the ocean, the specific humidity gradually increases along the trajectory until its proximity to the destination where rainout effect overrides recycling. For example, the specific humidity starts to decrease about 30 h before it arrives at PK (oceanic station), a delay of approximately 3 days at NK (inland station) (Supplementary Fig. S4). For PK site, both the precipitable water and OLR increase all the way towards the site, suggesting stronger convective recycling than rainout effect (Supplementary Fig. S6 and Fig. S7). For NK site in May, due to rainfall at the southwest coast before the airmass landed, there is indeed a decrease in precipitable water from 53.5 kg m^{-2} to 51.8 kg m^{-2} (Supplementary Fig. S6), and also an increase in OLR from 190.4 W m^{-2} to 204.9 W m^{-2} (Supplementary Fig. S7). On the other hand, for NK site in Sep, as mentioned earlier, land surface evapotranspiration serves as an important source of water vapor. The precipitable water content increases slightly from 52.6 kg m^{-2} to 52.9 kg m^{-2} after the air mass landed, accompanied by a decrease in OLR from 203.5 W m^{-2} to 188.6 W m^{-2} .

The case of the NK site in May showed more complex variations than other cases. As shown in Fig. 6 and Supplementary Figure S4, during the rainout period (-100 h to 0 h), $\delta^{18}\text{O}$ did not decrease with increasing precipitable water and there was no significant correlation between $\delta^{18}\text{O}$ and OLR. The poor correlation between precipitable water and $\delta^{18}\text{O}$ is generally contrary to so-called amount effect.

One potential reason for the poor correlation at NK in May may be related to the model that cannot effectively estimate moisture sources due to air mass advection from other source regions. The back-trajectory analysis showed that the Bay of Bengal, in the latitude band of 5° – 10°N , was a major source of moisture for NK in May. On the other hand, cluster means of OLR were lower than in other cases. As noted by Gadgil (2003), large-scale convection is likely to occur if SST is greater than 27.5°C and the OLR is less than 240 W m^{-2} . In this case, OLR varied between 210 and 240 W m^{-2} and SST in this source region was about 29.6°C , suggesting the region was dominated by large-scale convection for the whole period. Under such conditions, the surface solar radiation is decreased by cloud cover, thus reducing local evaporation. Therefore, the rapid increase of specific humidity along its trajectory between -222 h and -102 h (Supplementary Fig. S4) was less

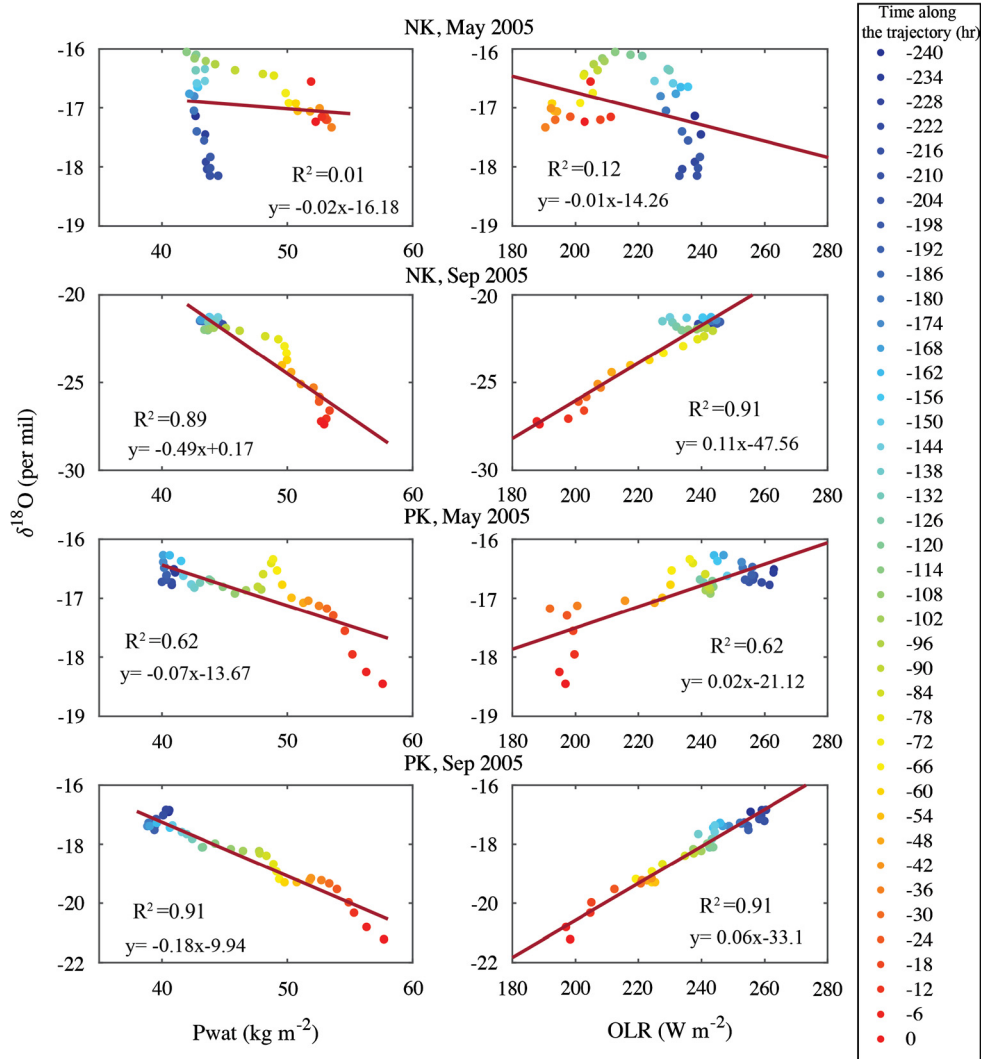


Fig. 6. Time evolution of IsoGSM-simulated precipitable water, its $\delta^{18}\text{O}$ and outgoing longwave radiation along the airmass back trajectory, and their correlations for NK and PK in May and September.

likely to be caused by the local evaporation in the source region and more likely to be caused by advection of moisture from other regions. We did similar analysis for the cases of May 2004 and 2006. We found that although OLR was 180–280 W m^{-2} , which is higher than that in May 2005, and with the evaporation source closer to the Bay of Bengal, the correlation between OLR and $\delta^{18}\text{O}$ only showed limit improvement ($R^2 = 0.35$ and $R^2 = 0.25$ for May 2004 and 2006, respectively).

Rain re-evaporation during rain-out process may have also contributed to the water vapor isotopic variations. However, this process would reduce the isotope ratio of the remaining vapor, which is contradictory with our results. A more reasonable explanation is that $\delta^{18}\text{O}$ is affected by mixing of moisture originated from several sources during the rain-out process, leading to more enriched $\delta^{18}\text{O}$ of water vapor. The IsoGSM produced relatively higher $\delta^{18}\text{O}$ of precipitable water (-13.0‰) northward of the Bay of Bengal ($16^\circ\text{--}20^\circ\text{N}$). With mixing of air masses in this region, $\delta^{18}\text{O}$ would not strictly follow the Rayleigh distillation prediction.

Another potential reason comes from biases of IsoGSM simulation. In this case, the moisture forming precipitation came largely from the Bay of Bengal, while for other cases the moisture pathway crossed the Indian Ocean, the Arabian Sea and Northwest Pacific. The longer transport distance allowed for enhanced Rayleigh distillation during the moisture transport and hence for isotopic deple-

tion in precipitable water, thus improving the precision of model simulation.

Nevertheless, our analysis indicates that the rain-out history of the air masses and the moisture source are major factors that control the precipitation $\delta^{18}\text{O}$ variability, in parallel with the local amount effect. These two controlling factors are reflected by large-scale convective activity along the storm trajectory.

Fig. 7 illustrates climatological mean variations in the source proportions for the rainy season. The Indian Ocean was the dominant moisture source during the summer monsoon season (May–August) for all the sites, contributing to more than 70% of the total moisture. In the pre-monsoon (April) and the post-monsoon (September–October) seasons, either the western North Pacific or the land surface played a dominant role. As shown in Figs. 1 and 7, the corresponding moisture source patterns changed seasonally and among the observation sites, contributing to the spatial difference of precipitation isotopic compositions at our sites. For the same month, the spatial difference of observed precipitation $\delta^{18}\text{O}$ can be attributed to moisture source and rain-out history. For example, in April, because of high contribution of low-latitude Pacific source (with high ET $\delta^{18}\text{O}$, see Supplementary Fig. S8), the PK site showed the highest precipitation $\delta^{18}\text{O}$ (Fig. 3). However, because of the lack of contribution from high latitude Indian Ocean source (with low ET $\delta^{18}\text{O}$), lower precipitation $\delta^{18}\text{O}$ values were

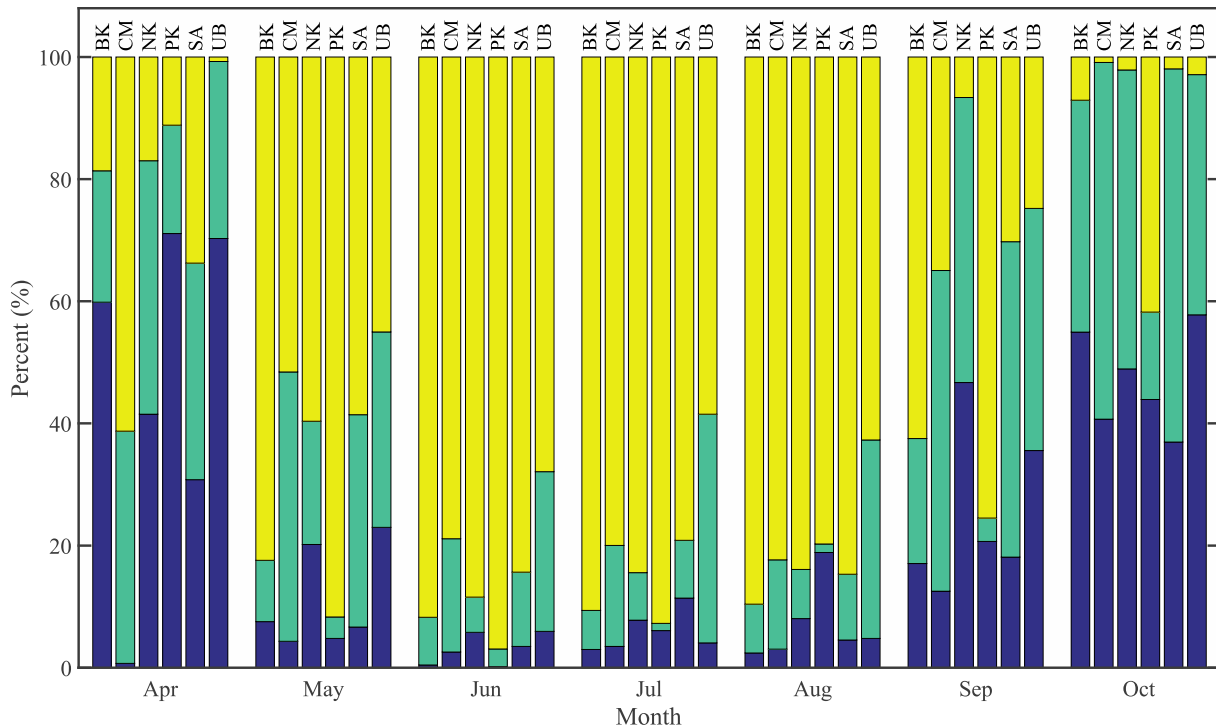


Fig. 7. The multi-year (2003–2013) mean fractional contribution to atmospheric moisture at each site. Yellow color represents source from Indian Ocean; green color represents source from Land surface and blue color represent source from Pacific Ocean.

observed at the UB and BK sites. For the SA, CM and NK sites, on the other hand, the most depleted precipitation $\delta^{18}\text{O}$ values were observed due largely to the proximity to high latitude Indian Ocean and adjacent land. In the summer monsoon season, in contrast to the Pacific-sourced moisture, precipitation controlled by the Indian Ocean source has relatively depleted ET $\delta^{18}\text{O}$. As shown in Supplementary Figure S8, from May to August, the Indian Ocean ET $\delta^{18}\text{O}$ is about 6‰ lower than that of the Pacific Ocean. In September, precipitation $\delta^{18}\text{O}$ was low, which probably reflects the dominance of the ^{18}O -depleted land surface evaporation (Fig. S8). Therefore, the spatial difference of precipitation $\delta^{18}\text{O}$ can be partly attributed to different moisture sources. The source effect is also supported by d-excess analysis. During the monsoon season, due to the dominant role of the Indian Ocean moisture source, the observed precipitation d-excess value was highly consistent with those of source water, as precipitation d-excess decreased with decreasing ET d-excess, as shown in Supplementary Figure S9. It is noted that for the pre-monsoon and post-monsoon seasons, d-excess analysis become less reliable due to the influence of rain drop re-evaporation.

On the other hand, as the air-mass moved inland along the monsoon track, precipitation $\delta^{18}\text{O}$ became gradually depleted with the progressive rainout: NK, the furthest inland station, had the lowest summer precipitation $\delta^{18}\text{O}$ values among all sites (Fig. 3). Therefore, during the rainy season (April–October), both source and rain-out effect can greatly alter observed precipitation $\delta^{18}\text{O}$ in different sites for a given month, but the convective-driven rainout that alters precipitable water $\delta^{18}\text{O}$ along the trajectory appears to play a more important role. For example, although the IsoGSM simulated an increase in the ET $\delta^{18}\text{O}$ from May to August over the Indian Ocean, the observed precipitation isotopes showed a decreased trend.

Fig. 8 shows the long term (2003–2012) spatial distribution of the correlation coefficient between the monthly OLR and precipitation $\delta^{18}\text{O}$ observed at each of the six sites. Positive correlation is evident in the large convective zone spanning from the Bay

of Bengal in the west to the South China Sea in the east. Large-scale atmospheric circulations can cause homogeneous changes in cloud-related variables, such as CTP and CTP, in the south Asia region (Cai and Tian, 2016a, 2016b), resulting in the consistency in the spatial pattern of the correlation coefficients between the $\delta^{18}\text{O}$ and convective activity in the ITCZ region. At the oceanic island station (PK), precipitation $\delta^{18}\text{O}$ correlated significantly with OLR at the local grid ($R = 0.64$). At the inland stations NK and SA, even though the correlation between $\delta^{18}\text{O}$ and OLR at the local grid was weak ($R = 0.18$ for NK and $R = 0.32$ for SA), the correlation between $\delta^{18}\text{O}$ and OLR showed similar spatial patterns to that for UB, with the highest correlation found in the ITCZ zone ($R = 0.72$ for NK and $R = 0.57$ for SA). The strong correlations of monthly $\delta^{18}\text{O}$ with local precipitation (except for the NK site) and with OLR emphasize that isotopic variability of precipitation is not only related to local precipitation amount, but also to large-scale organized convection activity.

The location at which the correlation between the $\delta^{18}\text{O}$ and OLR is the highest is indicative of the dominant moisture source. At CM, although the Indian Ocean was the dominant source during the monsoon season (Fig. 7), precipitation $\delta^{18}\text{O}$ in this site had a higher correlation with OLR in the South China Sea than in the Indian Ocean. This is because the data gap resulted in a higher proportion (53%) of months that were controlled more by the Pacific monsoon (east of 100°E , non-summer cases) than by the Indian monsoon (west of 100°E , mainly summer cases). If we selected the summer season (May–Aug.) only, the highest spatial correlation R would improve from 0.79 to 0.84 and the location of the highest correlation would be in the Bay of Bengal. For the winter season (December–January–February, DJF) when precipitation was weak (Fig. 3), the model simulation indicated different sources of moisture among different sites (Fig. 1). For the PK site, there was a significant moisture contribution from the Pacific Ocean, with a high correlation between $\delta^{18}\text{O}$ and OLR occurring in the Pacific Ocean. Although high correlations also existed over the South Indian Ocean and the land surface, these

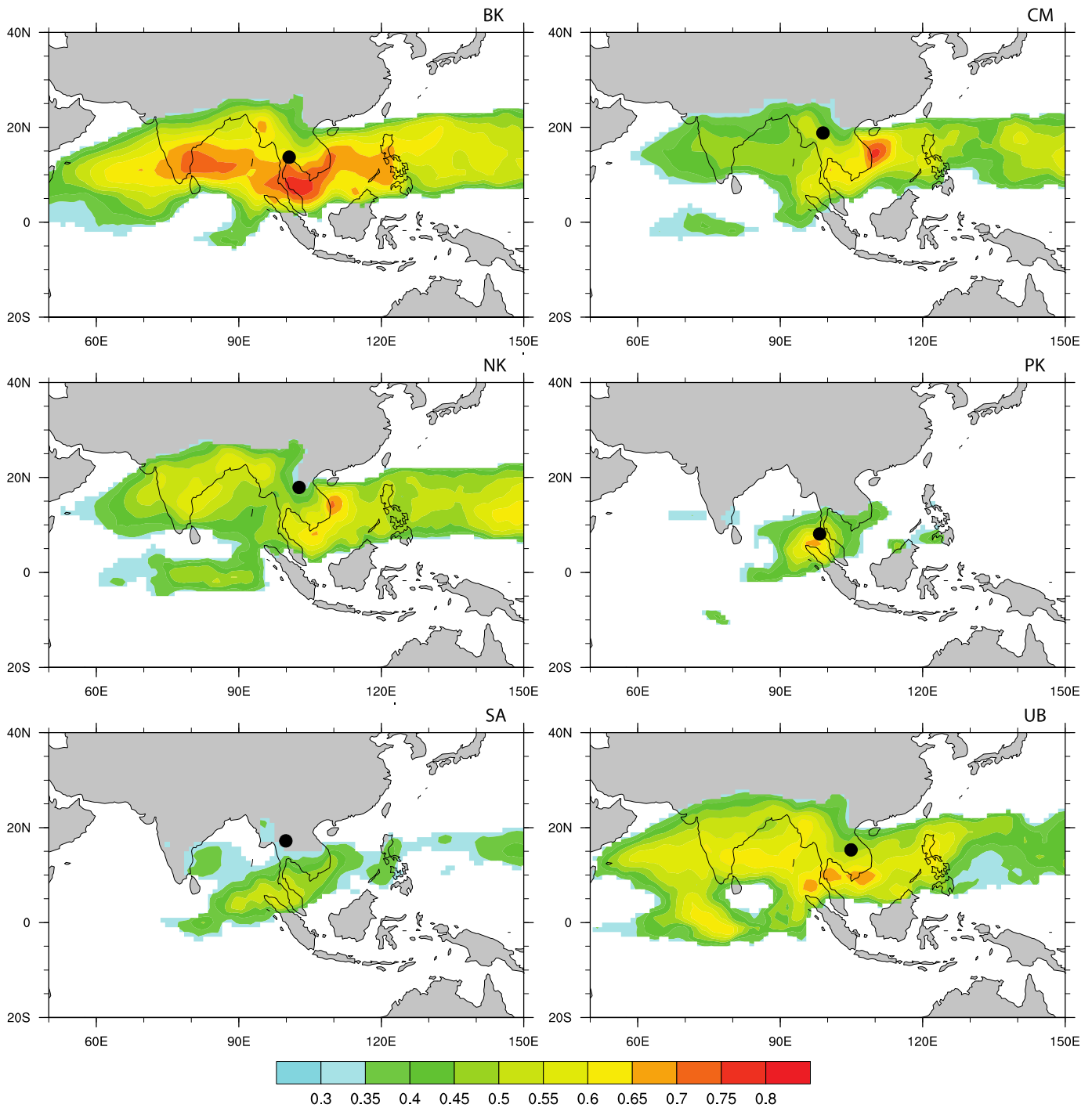


Fig. 8. Spatial distribution of correlation coefficients (R) between monthly precipitation $\delta^{18}\text{O}$ and OLR. Only areas with $R > 0.3$ are shown.

correlations may be misleading considering the moisture transport path (Supplementary Fig. S10 and Fig. 1). For the BK and the CM site, flows from the Pacific Ocean and the Indian Ocean played equally dominant roles. Thus the correlation between $\delta^{18}\text{O}$ and OLR showed similar spatial patterns (Supplementary Fig. S10) to those shown in Fig. 8. On the other hand, sources of water vapor for UB, NA and SA were dominated by land contributions. The highest correlations between $\delta^{18}\text{O}$ and OLR were found in inland areas (along the moisture transport path, except the UB site due to lack of data). Nevertheless, these results further highlight that precipitation $\delta^{18}\text{O}$ was associated with the moisture source and large-scale convective activity along the airmass trajectory.

4. Conclusions

In this study, we presented multi-year long time series of monthly rainfall $\delta^{18}\text{O}$ observed at six sites in Thailand, aiming to investigate the processes controlling temporal and spatial isotopic variability in this region. We compared rainfall $\delta^{18}\text{O}$ to local atmospheric variables, including precipitation amount, temperature, and activity of convection. With the help of a Lagrangian moisture source diagnostic tool (HYSPPLIT) and an isotope-enabled GCM (IsoGSM), large-scale convection and moisture source region that drive monthly isotopic variability were also investigated.

Different from existing interpretation, such as the inverse relationship between rainfall $\delta^{18}\text{O}$ and precipitation amount, known

as the amount effect, we found that the spatial and temporal changes in the stable isotope ratios of precipitation depended both on the seasonal dynamics of moisture sources and that associated large scale convection patterns and local precipitation amount. Both moisture source analysis and IsoGSM simulation showed that the observed winter-enriched/summer-depleted seasonal distribution of precipitation $\delta^{18}\text{O}$ at all the sites was controlled by convective activity altering precipitable water $\delta^{18}\text{O}$ along the trajectory.

The spatial variability of precipitation $\delta^{18}\text{O}$ among the observation network was highly dependent on fractional contribution of different moisture sources. For example, the precipitation $\delta^{18}\text{O}$ at NK in September 2015 was lower than that at PK in the same month, because lower contribution of moisture source from Indian Ocean. Strong positive correlation was found between local precipitation $\delta^{18}\text{O}$ observed at all the six sites and the outgoing longwave radiation (OLR) in the large convective zone spanning from the Bay of Bengal in the west to the South China Sea in the east, reflecting the impact of large scale convective activity.

Acknowledgements

HYSPLIT back-trajectory model and the relevant input datasets were obtained from the NOAA Air Resources Laboratory for making available the GPCP and TRMM Precipitation data and OLR data were provided by the NOAA/OAR/ESRL PSD, Boulder, Colorado, USA. AIRS cloud products were distributed by the NASA Goddard Earth Sciences Data Information and Services Center (GESDISC). This research was supported by the Environment Research and Technology Development Fund (2-1503 and S-12) of Environmental Restoration and Conservation Agency, the Japanese Society for the Promotion of Science (Grants 15KK0199 and 16H06291), the SOUSEI Program, the ArCS and TOUGOU projects of MEXT, and the U.S. National Science Foundation (Grant AGS-1520684). All the data used in this study are available on request from the corresponding author.

Appendix A. Supplementary material

Supplementary material related to this article can be found online at <https://doi.org/10.1016/j.epsl.2018.02.015>.

References

- Adler, R.F., Huffman, G.J., Chang, A., Ferraro, R., Xie, P.-P., Janowiak, J., Rudolf, B., Schneider, U., Curtis, S., Bolvin, D., Gruber, A., Susskind, J., Arkin, P., Nelkin, E., 2003. The version-2 Global Precipitation Climatology Project (GPCP) monthly precipitation analysis (1979–Present). *J. Hydrometeorol.* 4, 1147–1167.
- Aemisegger, F., Pfahl, S., Sodemann, H., Lehner, I., Seneviratne, S.I., Wernli, H., 2014. Deuterium excess as a proxy for continental moisture recycling and plant transpiration. *Atmos. Chem. Phys.* 14, 4029–4054.
- Aggarwal, P.K., Frohlich, K., Kulkarni, K.M., Gourcy, L.L., 2004. Stable isotope evidence for moisture sources in the Asian summer monsoon under present and past climate regimes. *Geophys. Res. Lett.* 31, L08203.
- Aggarwal, P.K., Romatschke, U., Araguas-Araguas, L., Belachew, D., Longstaffe, F.J., Berg, P., Schumacher, C., Funk, A., 2016. Proportions of convective and stratiform precipitation revealed in water isotope ratios. *Nat. Geosci.* 9, 624–629.
- Araguás-Araguás, L., Froehlich, K., Rozanski, K., 1998. Stable isotope composition of precipitation over southeast Asia. *J. Geophys. Res., Atmos.* 103, 28721–28742.
- Breitenbach, S.F.M., Adkins, J.F., Meyer, H., Marwan, N., Kumar, K.K., Haug, G.H., 2010. Strong influence of water vapor source dynamics on stable isotopes in precipitation observed in Southern Meghalaya, NE India. *Earth Planet. Sci. Lett.* 292, 212–220.
- Cai, Z., Tian, L., 2016a. Processes governing water vapor isotope composition in the Indo-Pacific region: convection and water vapor transport. *J. Climate* 29, 8535–8546.
- Cai, Z.Y., Tian, L.D., 2016b. Atmospheric controls on seasonal and interannual variations in the precipitation isotope in the East Asian Monsoon region. *J. Climate* 29, 1339–1352.
- Craig, H., 1961. Isotopic variations in meteoric waters. *Science* 133, 1702–1703.
- Crawford, J., Hollins, S.E., Meredith, K.T., Hughes, C.E., 2017. Precipitation stable isotope variability and subcloud evaporation processes in a semi-arid region. *Hydrol. Process.* 31, 20–34.
- Crawford, J., Hughes, C.E., Parkes, S.D., 2013. Is the isotopic composition of event based precipitation driven by moisture source or synoptic scale weather in the Sydney Basin, Australia? *J. Hydrol.* 507, 213–226.
- Dansgaard, W., 1964. Stable isotopes in precipitation. *Tellus* 16, 436–468.
- Draxler, R.R., Hess, G.D., 1997. Description of the HYSPLIT4 Modeling System. Tech. Rep. ERL ARL-230D, NOAA Tech. Memo, 1999.
- Farlin, J., Lai, C.-T., Yoshimura, K., 2013. Influence of synoptic weather events on the isotopic composition of atmospheric moisture in a coastal city of the western United States. *Water Resour. Res.* 49, 3685–3696.
- Funk, A., Schumacher, C., Awaka, J., 2013. Analysis of rain classifications over the tropics by Version 7 of the TRMM PR 2A23 algorithm. *J. Meteorol. Soc. Jpn. Ser. II* 91, 257–272.
- Gat, J.R., 2000. Atmospheric water balance—the isotopic perspective. *Hydrol. Process.* 14, 1357–1369.
- He, Y., Risi, C., Gao, J., Masson-Delmotte, V., Yao, T.D., Lai, C.T., Ding, Y.J., Worden, J., Frankenberg, C., Chepfer, H., Cesana, G., 2015. Impact of atmospheric convection on south Tibet summer precipitation isotopologue composition using a combination of in situ measurements, satellite data, and atmospheric general circulation modeling. *J. Geophys. Res., Atmos.* 120, 3852–3871.
- Kahn, B.H., Chahine, M.T., Stephens, G.L., Mace, G.G., Marchand, R.T., Wang, Z., Barnett, C.D., Eldering, A., Holz, R.E., Kuehn, R.E., Vane, D.G., 2008. Cloud type comparisons of AIRS, CloudSat, and CALIPSO cloud height and amount. *Atmos. Chem. Phys.* 8, 1231–1248.
- Kurita, N., Ichiyanagi, K., Matsumoto, J., Yamanaka, M.D., Ohata, T., 2009. The relationship between the isotopic content of precipitation and the precipitation amount in tropical regions. *J. Geochim. Explor.* 102, 113–122.
- Lawrence, J.R., Gedzelman, S.D., Dexheimer, D., Cho, H.K., Carrie, G.D., Gasparini, R., Anderson, C.R., Bowman, K.P., Biggerstaff, M.I., 2004. Stable isotopic composition of water vapor in the tropics. *J. Geophys. Res., Atmos.* 109, D06115.
- Lekshmy, P.R., Midhun, M., Ramesh, R., Jani, R.A., 2014. ^{18}O depletion in monsoon rain relates to large scale organized convection rather than the amount of rainfall. *Sci. Rep.* 4, 5661.
- Leng, M.J., Marshall, J.D., 2004. Palaeoclimate interpretation of stable isotope data from lake sediment archives. *Quat. Sci. Rev.* 23, 811–831.
- Liebmann, B., Smith, C.A., 1996. Description of a complete (interpolated) outgoing longwave radiation dataset. *Bull. Am. Meteorol. Soc.* 77, 1275–1277.
- Liu, Z., Yoshimura, K., Bowen, G.J., Buening, N.H., Risi, C., Welker, J.M., Yuan, F., 2014. Paired oxygen isotope records reveal modern North American atmospheric dynamics during the Holocene. *Nat. Commun.* 5, 3701 (7 pp.).
- Mook, W.G., 2000. Environmental Isotopes in Hydrological Cycle: Principles and Applications, IHP-V. Technical Documents in Hydrology. UNESCO/IAEA.
- Moore, M., Kuang, Z., Blossey, P.N., 2014. A moisture budget perspective of the amount effect. *Geophys. Res. Lett.* 41, 1329–1335.
- Pang, H., Hou, S., Kaspari, S., Mayewski, P.A., 2014. Influence of regional precipitation patterns on stable isotopes in ice cores from the central Himalayas. *Cryosphere* 8, 289–301.
- Pfahl, S., Wernli, H., Yoshimura, K., 2012. The isotopic composition of precipitation from a winter storm – a case study with the limited-area model COSMOiso. *Atmos. Chem. Phys.* 12, 1629–1648.
- Risi, C., Bony, S., Vimeux, F., 2008. Influence of convective processes on the isotopic composition ($\delta^{18}\text{O}$ and δD) of precipitation and water vapor in the tropics, 2: physical interpretation of the amount effect. *J. Geophys. Res.* 113, D19306.
- Risi, C., Bony, S., Vimeux, F., Frankenberg, C., Noone, D., Worden, J., 2010. Understanding the Sahelian water budget through the isotopic composition of water vapor and precipitation. *J. Geophys. Res., Atmos.* 115, D24110.
- Risi, C., Noone, D., Frankenberg, C., Worden, J., 2013. Role of continental recycling in intraseasonal variations of continental moisture as deduced from model simulations and water vapor isotopic measurements. *Water Resour. Res.* 49, 4136–4156.
- Royle, J., Sime, L.C., Hodgson, D.A., Convey, P., Griffiths, H., 2013. Differing source water inputs, moderated by evaporative enrichment, determine the contrasting $\delta^{18}\text{O}$ CELLULOSE signals in maritime Antarctic moss peat banks. *J. Geophys. Res., Biogeosci.* 118, 184–194.
- Rozanski, K., Araguás-Araguás, L., Gonfiantini, R., 1993. Isotopic Patterns in Modern Global Precipitation.
- Sodemann, H., Masson-Delmotte, V., Schwierz, C., Vinther, B.M., Wernli, H., 2008. Interannual variability of Greenland winter precipitation sources, 2: effects of North Atlantic Oscillation variability on stable isotopes in precipitation. *J. Geophys. Res., Atmos.* 113, D12111.
- Stein, A.F., Draxler, R.R., Rolph, G.D., Stunder, B.J.B., Cohen, M.D., Ngan, F., 2015. NOAA's HYSPLIT atmospheric transport and dispersion modeling system. *Bull. Am. Meteorol. Soc.* 96, 2059–2077.
- Tang, Y., Pang, H., Zhang, W., Li, Y., Wu, S., Hou, S., 2015. Effects of changes in moisture source and the upstream rainfall on stable isotopes in summer precipitation – a case study in Nanjing, East China. *Hydrol. Earth Syst. Sci.* 12, 3919–3944.
- Tremoy, G., Vimeux, F., Soumana, S., Souley, I., Risi, C., Favreau, G., Oi, M., 2014. Clustering mesoscale convective systems with laser-based water vapor $\delta^{18}\text{O}$ monitoring in Niamey (Niger). *J. Geophys. Res., Atmos.* 119, 5079–5103.
- Trenberth, K.E., 1998. Atmospheric moisture residence times and cycling: implications for rainfall rates and climate change. *Clim. Change* 39 (4), 667–694.

- Uemura, R., Yonezawa, N., Yoshimura, K., Asami, R., Kadena, H., Yamada, K., Yoshida, N., 2012. Factors controlling isotopic composition of precipitation on Okinawa Island, Japan: implications for paleoclimate reconstruction in the East Asian Monsoon region. *J. Hydrol.* 475, 314–322.
- Wang, S.J., Zhang, M.J., Che, Y.J., Chen, F.L., Qiang, F., 2016a. Contribution of recycled moisture to precipitation in oases of arid central Asia: a stable isotope approach. *Water Resour. Res.* 52, 3246–3257.
- Wang, S.J., Zhang, M.J., Che, Y.J., Zhu, X.F., Liu, X.M., 2016b. Influence of below-cloud evaporation on deuterium excess in precipitation of Arid Central Asia and its meteorological controls. *J. Hydrometeorol.* 17, 1973–1984.
- Wang, S.J., Zhang, M.J., Crawford, J., Hughes, C.E., Du, M.X., Liu, X.M., 2017. The effect of moisture source and synoptic conditions on precipitation isotopes in arid central Asia. *J. Geophys. Res., Atmos.* 122, 2667–2682.
- Wei, Z., Yoshimura, K., Okazaki, A., Ono, K., Kim, W., Yokoi, M., Lai, C.-T., 2016. Understanding the variability of water isotopologues in near-surface atmospheric moisture over a humid subtropical rice paddy in Tsukuba, Japan. *J. Hydrol.* 533, 91–102.
- Xie, L., Wei, G., Deng, W., Zhao, X., 2011. Daily $\delta^{18}\text{O}$ and δD of precipitations from 2007 to 2009 in Guangzhou, South China: implications for changes of moisture sources. *J. Hydrol.* 400, 477–489.
- Yang, X.X., Yao, T.D., Yang, W.L., Xu, B.Q., He, Y., Qu, D.M., 2012. Isotopic signal of earlier summer monsoon onset in the bay of Bengal. *J. Climate* 25, 2509–2516.
- Yoshimura, K., Kanamitsu, M., Noone, D., Oki, T., 2008. Historical isotope simulation using reanalysis atmospheric data. *J. Geophys. Res., Atmos.* 113, D19108.
- Yoshimura, K., Miyoshi, T., Kanamitsu, M., 2014. Observation system simulation experiments using water vapor isotope information. *J. Geophys. Res., Atmos.* 119, 7842–7862.
- Yoshimura, K., Oki, T., Ohte, N., Kanae, S., 2003. A quantitative analysis of short-term ^{18}O variability with a Rayleigh-type isotope circulation model. *J. Geophys. Res., Atmos.* 108.
- Zwart, C., Munksgaard, N.C., Kurita, N., Bird, M.I., 2016. Stable isotopic signature of Australian monsoon controlled by regional convection. *Quat. Sci. Rev.* 151, 228–235.